

# Demonstration of Reversible Dispersion in a Darcy-Scale Push-Pull Laboratory Experiment

Roseanna M. Neupauer<sup>1</sup> · Eric J. Roth<sup>1,2</sup> · John P. Crimaldi<sup>1</sup> · David C. Mays<sup>4</sup> · Lauren J. Sather<sup>1,3</sup>

Received: 16 May 2021 / Accepted: 25 August 2021 © The Author(s), under exclusive licence to Springer Nature B.V. 2021

#### Abstract

A solute transport experiment was conducted in a  $50 \text{ cm} \times 50 \text{ cm} \times 4.4 \text{ cm}$  apparatus filled with monodisperse glass beads and glycerin, using Rhodamine 6G dye as the solute. The dye movement was tracked through two cycles of a push-pull flow pattern, alternating between approximately radial outward flow and approximately radial inward flow. Depth-averaged concentration was measured during the experiment and integrated over the angular direction during post-processing to obtain a radial distribution of concentration. The experimental results were replicated using particle tracking, simulating advection and dispersion in the radial direction, including reversible dispersion during extraction. Results show that spreading of the measured concentrations follow a Fickian dispersion model during steps with radial outward flow. During steps with radial inward flow, spreading is reversed and can be modeled as reversible dispersion. The observed reversal in spreading is an indication of incomplete mixing within the pore space.

**Keywords** Incomplete pore-scale mixing  $\cdot$  Fickian dispersion  $\cdot$  Radial flow  $\cdot$  Particle tracking  $\cdot$  Reversible dispersion

Roseanna M. Neupauer neupauer@colorado.edu

Eric J. Roth eric.roth@colorado.edu

John P. Crimaldi crimaldi@colorado.edu

David C. Mays david.mays@ucdenver.edu

Lauren J. Sather lauren.reising@colorado.edu

Published online: 09 September 2021

- University of Colorado Boulder, 1111 Engineering Dr., UCB 428, Boulder, Colorado 80309-0428, USA
- Present Address: University of Colorado Anschutz Medical Campus, Aurora, CO, USA
- Present Address: West Yost Associates, Lake Forest, CA, USA
- <sup>4</sup> University of Colorado Denver, Campus Box 113, PO Box 173364, Denver, CO 80217-3364, USA



#### 1 Introduction

Dissolved solutes in porous media are transported by advection of the pore fluid. Within the pore space, velocity varies with distance from the solid grain and the size and shape of the pore. Thus, the movement of individual parcels of fluid and dissolved solute is controlled by the geometry of the pore space. If the sub-pore-scale solute concentration is upscaled to the Darcy and larger scales, in effect sampling over many streamlines, the different velocities of individual solute parcels manifest as solute spreading at the larger scale. We use the term 'upscaled concentration' to describe concentration that is measured or calculated over a sample volume of multiple pores.

Incomplete mixing at the pore scale has been observed directly in an experimental apparatus. de Anna et al. (2014) constructed a two-dimensional Hele-Shaw cell with circular obstructions that represented grains. Solute and water were introduced separately into one end, and unidirectional flow was imposed. Solute concentration was imaged across the apparatus using a pixel area smaller than a pore, showing isolated regions with and without solute, thereby demonstrating incomplete mixing.

Experiments have also shown that if concentrations are averaged over multiple pores containing solute that is incompletely mixed, the spreading in the resulting concentration distribution may follow a Fickian dispersion model. de Anna et al (2014) averaged concentration in the direction transverse to flow in the Hele-Shaw cell over multiple (on the order of five or more) pores, and obtained a concentration distribution that matched a solution of the advection dispersion equation with Fickian dispersion. Gramling et al (2002) introduced solute continuously into a 36 cm-long chamber with a rectangular cross section of 5.5 cm × 1.8-cm filled with cryolite sand. Concentration of the solute was measured over the cross section perpendicular to flow and was shown to follow a Fickian dispersion model along the column length.

Gramling et al (2002) demonstrated incomplete mixing indirectly by introducing two reactive solutes into the chamber and measuring the concentration of the product over a sample volume of multiple pores. If the reactants were completely mixed in the pore space, the Fickian dispersion model would accurately represent the upscaled concentrations, and would be able to predict the upscaled concentration of the product. However the Fickian model overpredicted the actual concentration of the reaction product, indirectly demonstrating the reactants were not completely mixed within the pores. Incomplete mixing was also observed in a column experiment by Raje and Kapoor (2000), who introduced two reactive solutes into a column and measured the concentration of the reaction product in the column effluent. The product concentration was less than what would be predicted by a Fickian dispersion model, again indirectly demonstrating incomplete mixing. de Anna et al (2014) found similar results with reaction solutes in their Hele-Shaw experiment.

The previous experiments considered unidirectional, steady flow. In this paper, we demonstrate incomplete pore-scale mixing of a single solute in Darcy scale experiments with push-pull radial flow in a quasi-two-dimensional porous medium. The flow reversal in the push-pull experiment allows us to demonstrate incomplete pore-scale mixing by evaluating the Fickian dispersion model of the upscaled concentrations of a single solute, unlike the experiments of Raje and Kapoor (2000) and Gramling et al (2002), which required two reactive solutes to demonstrate incomplete mixing based on measured upscaled concentrations. The incomplete mixing leads to reversal of dispersion during the pull phase of the push-pull flow, which is consistent with field observations of breakthrough curves in a push-pull experiment in a fractured medium (Kang et al 2015).



To analyze the solute behavior in our push-pull experiment, we replicate the experimental results using one-dimensional particle tracking in the radial direction, including reversed dispersion during extraction. The comparison of numerical and experimental results allow us to draw conclusions about pore-scale mixing from the apparent Darcy-scale dispersion.

# 2 Experimental Investigation

In this experiment, laser-induced fluorescence is used to track the movement of a plume of fluorescent solute through refractive-index-matched (RIM) porous media and pore fluid. For a complete description of the experimental setup and procedure, the reader is directed to Roth et al (2021). This section presents the key points from Roth et al (2021) that are important for the present study.

#### 2.1 Experimental Setup

The experimental apparatus (Fig. 1) is an acrylic box that is 50 cm  $\times$  50 cm in the horizontal plane and 4.4 cm tall. The apparatus contains five fully penetrating wells that were fabricated from perforated tubing (Perforated Tubes Inc., code 70), with an outer diameter of 6.35 mm, and approximately 70% of the surface area open to flow. Well W5 is located in center of the apparatus, and the remaining four wells (W1–W4) are equally spaced on a circle of radius L=11.6 cm centered at well W5 (Fig. 1) (Roth et al 2021).

The RIM pair used in the experiment was borosilicate glass beads (porous medium) and glycerin (pore fluid), both of which have a refractive index of 1.447. The apparatus was filled with 16 layers of 3-mm-diameter beads (Pyrex, part# 7268-3), with hexagonal close packing (HCP) arrangement (Roth et al 2021). Along the bottom face, 1-mm-diameter beads (Chemglass, part# CG-1101-06) were placed in the pore space between the 3-mm-diameter beads to maintain relatively uniform porosity in the vertical column, that would otherwise be nonuniform due to the placement of spherical beads against a planar surface (Roth et al 2020). Along the upper face of the apparatus, the top three layers of beads were opaque (Roth et al 2021).

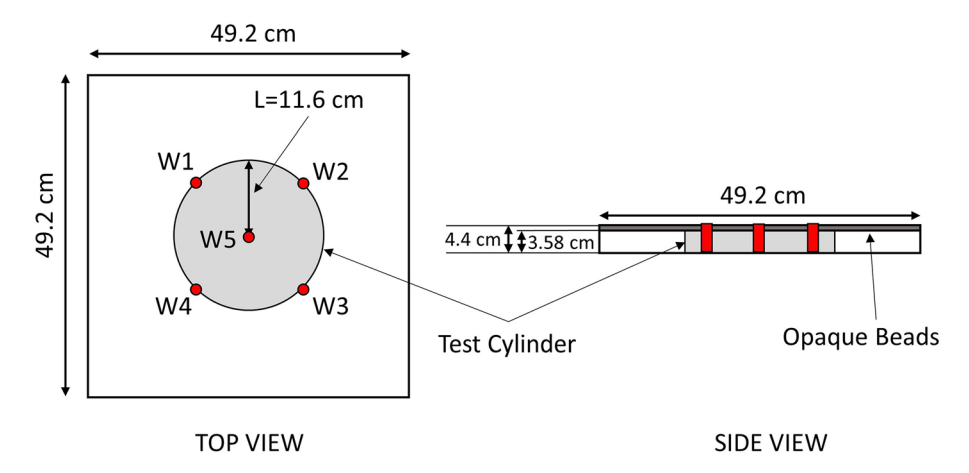


Fig. 1 Experimental apparatus with test cylinder (gray) and wells (red). Wells are not to scale

Rhodamine 6G (Aldrich, CAS# 989-38-8), which is soluble in glycerin, was used as the solute. Its diffusivity in glycerin is  $1.9 \times 10^{-9}$  cm<sup>2</sup>/s (Roth et al 2020), which leads to negligible molecular diffusion during the 120-minute experiments. During the experiment, the solute was illuminated with a 514-nm laser beam produced by an argon-ion laser (Coherent, Innova 90C-6, Santa Clara, CA) that was directed approximately normal to the bottom face of the apparatus. Images of the intensity of the solute concentration were captured at 15-second intervals using a camera (Imperx, Bobcat ICL-B1410M-SCO, Boca Raton, FL) that was fitted with an optical band-pass filter (Omega Optics, 555Df30, Austin, TX) that blocked the excitation light from the laser and transmitted light from the fluoresced solute. Each pixel (area of 0.0023 cm<sup>2</sup>) in the image captured the vertically integrated intensity over the total volume (pore space and beads) comprised by the lower 13 layers of beads. The images were corrected to account only for the pore volume, which is the volume that can be occupied by the solute. The top three layers of beads (out of 16 layers in total) were opaque and therefore were not part of the imaged volume, which eliminated any variability due to uneven bead alignment at the upper face of the apparatus. Because of the vertical integration over multiple pores, the images represent the Darcy-scale concentration (Roth et al 2021).

Although the images captured intensity over a 1040 x 1392 grid of pixels, the present study focuses on the behavior within the cylindrical volume of radius L=11.6 cm and centered at well W5 in the horizontal plane (excluding the area of the well W5), and with a height equivalent the imaged height (13/16 of the apparatus height, (13/16)(4.4 cm) = 3.58 cm). We call this volume the "test cylinder" (see Fig. 1). With these dimensions, the total volume of the test cylinder is  $1510 \text{ cm}^3$ .

The bead packing controls the porosity, with perfect HCP packing having a theoretical porosity of 0.26. The uniformity of the packing in the apparatus can be observed in the spatial distribution of vertically averaged porosity in the test cylinder, which was measured as described in Roth et al (2021) and is shown in Fig. 2. Spatial variation in porosity is unavoidable due to the circular shape of the wells which disrupts the hexagonal pattern of the bead packing, and the disruptions propagate away from the wells. Nevertheless, the porosity is relatively uniform across the test cylinder (Fig. 2a,b), with the porosity somewhat higher than the theoretical minimum for HCP. In the present study, we focus on radial movement of the solute, integrating over the angular direction across the test cylinder. The radial distribution of porosity, calculated from the images in Fig. 2a,b in Matlab using radialavg.m (Fischer 2019), is shown in Fig. 2c. The porosity is highest near well W5 and decreases to a relatively uniform value away from the well. The area-weighted average porosity for this bead packing arrangement was 0.311 (red dashed line in Fig. 2).

To begin the experiment, approximately 20 mL of a solute/glycerin solution with concentration of  $C_o=8$  mg/L of Rhodamine 6G was introduced manually into the apparatus through well W5 at a rate of approximately 4 mL/min, while expelling solute-free glycerin through the other four wells to conserve mass of fluid in the apparatus. The resulting solute distribution (see Figure 3a) is the initial solute distribution for the experiment Roth et al (2021).

## 2.2 Experimental Results

The push-pull experiment was conducted by alternately injecting glycerin and extracting fluid at well W5, using high-accuracy syringe pumps (Kd Scientific, Legato 270, Holliston, MA) programmed for the four-step flow sequence shown in Table 1. To minimize extraction of solute at well W5, the extraction rates in flow steps 2 and 4 are less than the injection rates in flow steps 1 and 3, respectively. To preserve fluid mass within



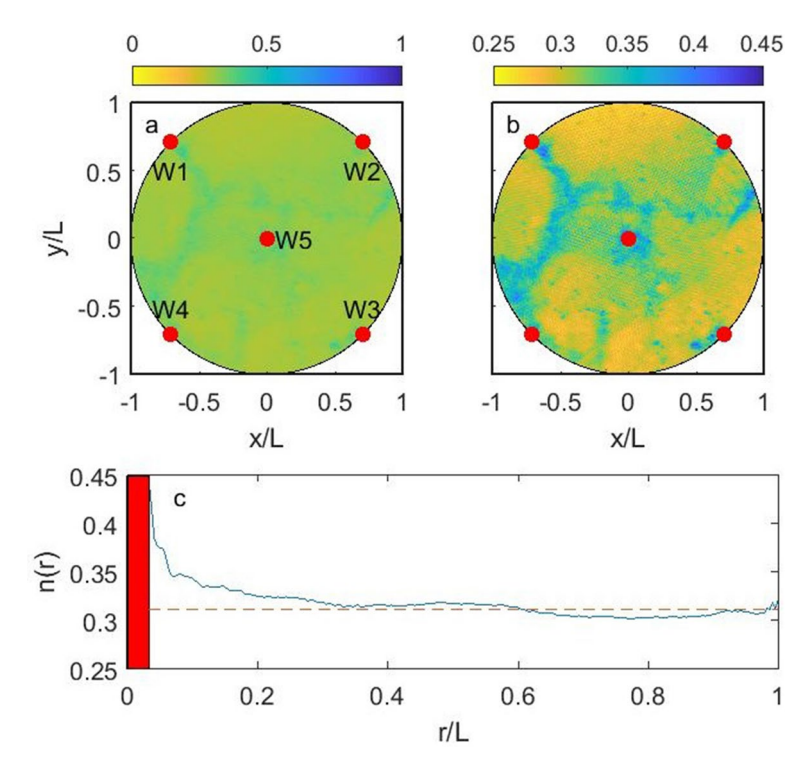


Fig. 2 Porosity, n, in the test cylinder. a Two-dimensional porosity distribution displayed with color range of  $0 < n \le 1$ . b Two-dimensional porosity distribution displayed with color range of  $0.25 < n \le 0.45$ . c Radial porosity distribution. Red circles and shading denote wells. The dashed red line represents the areal-averaged porosity

the apparatus, fluid was extracted at the four outer wells (W1–W4) during flow steps 1 and 3, at a rate equal to one fourth of the injection rate at well W5. Similarly, fluid was injected in well W1–W4 during flow steps 2 and 4. Although the flow conditions are not purely radial, the solute plume remains sufficiently far from the outer wells to experience approximately radial flow.

The Peclet number, Pe, is calculated for each flow step as

$$Pe = \frac{v(r)r}{D_m} = \frac{|Q_{5,J}|}{2\pi b n D_m} \tag{1}$$

where  $|Q_{5,J}|$  is the magnitude of the injection or extraction rate at Well W5 during flow step J, b = 4.4 cm is the thickness of the apparatus, n = 0.311 is the average porosity, and  $D_m = 1.9 \times 10^{-9}$  cm<sup>2</sup>/s (Roth et al 2020) is the molecular diffusion coefficient. The values, reported in Table 1, show that the experiment is strongly advection-controlled.

The solute distributions at the end of the four flow steps are shown in Figs. 3b—e. A movie of the experiment is available in Online Resource 1. The plume moved predominantly in the radial direction, although some variability is present, which is controlled by the local porosity (see Fig. 2a,b). Locally, the solute plume travels farther where porosity is higher, i.e., where the resistance to flow is low. Two replicates of



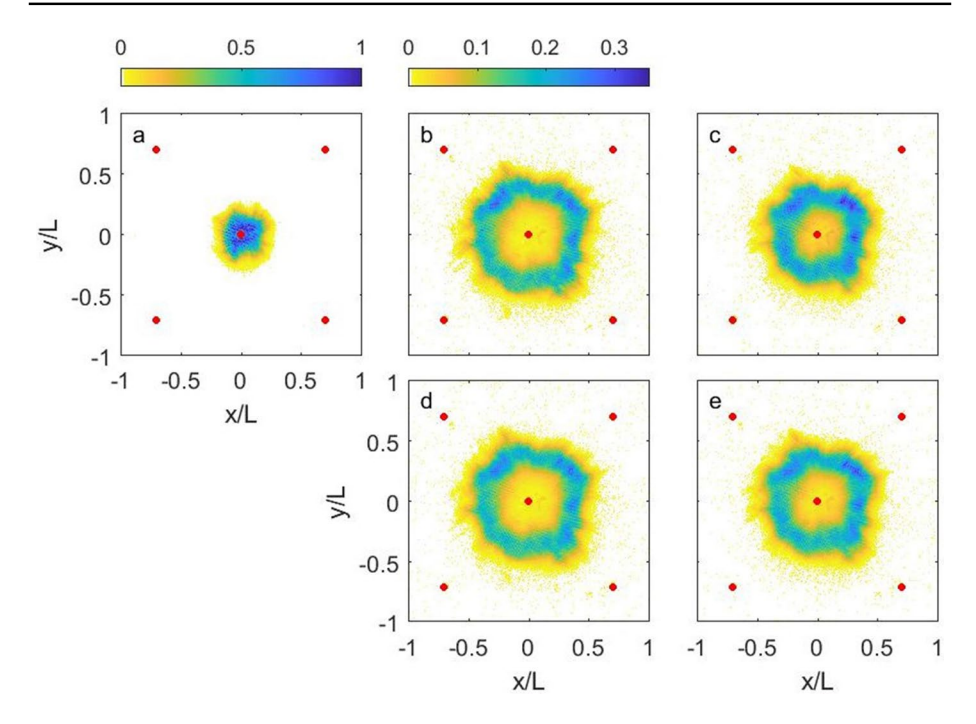


Fig. 3 Normalized dye concentration (normalized by  $C_o$ ) **a** at the start of the experiment, **b** at the end of Flow Step 1, **c** at the and of Flow Step 2, **d** at the end of Flow Step 3, and **e** at the end of Flow Step 4. Red circles represent well locations. The colorbar above subplot a applies to subplot a; the colorbar above subplot b applies to subplot b—e

**Table 1** Injection (positive) and extraction (negative) rates and durations of each flow step

Flow Step, J	Injection rate (mL/min)		Duration (min)	Pe
	Wells W1–W4	Well W5		
	$Q_{1,J}-Q_{4,J}$	$Q_{5,J}$		
1	-0.75	3.0	30	$3 \times 10^{6}$
2	0.25	-1.0	30	$1 \times 10^6$
3	-0.25	1.0	30	$1 \times 10^6$
4	0.125	-0.5	30	$5 \times 10^5$

the experiment were conducted and produced nearly identical results (Roth et al 2021); thus we only show the results of one replicate (Replicate 1, from Roth et al (2021)).

The total mass of solute in the test cylinder was calculated by

$$M(t) = \sum_{i \in r_w < r_i \le L} C(i, t) n_i b A$$
 (2)

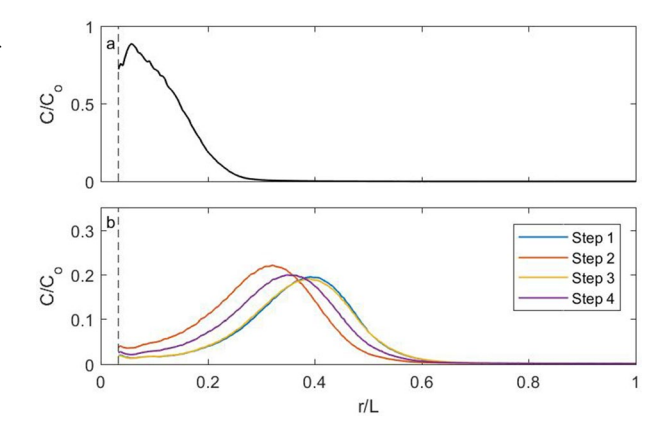
where M(t) is the mass of solute in the test cylinder at time t,  $r_w$  is the outer radius of the well,  $r_i$  is the radial distance from the center well to the center of pixel i, L=11.6 cm is the radial distance between the center well and the outer wells (i.e., the outer edge of the test



Fig. 4 Mass of dye in the test cylinder as a function of time. The red dotted line represents the simplified mass distribution matched in the numerical simulations. Vertical dotted lines represent start time of a new flow step

0.15 0.1 (gm) M 0.05 Sten 1 Sten 2 Sten 3 Sten 4 (extraction) (injection) (injection) (extraction) 0 0 15 30 45 60 75 90 105 120 t (min)

Fig. 5 Radial distribution of solute concentration **a** at the start of the experiment and **b** at the end of each flow step. The vertical dashed line represents the outer edge of well W5



cylinder), C(i,t) is the concentration in pixel i at time t,  $n_i$  is the porosity in pixel i, b is the imaged thickness, A=0.0023 cm² is the area of a pixel, and the summation is carried out over all pixels whose centers are within the test cylinder. Figure 4 shows the mass inside the test cylinder at 15-second intervals during the experiment. At the start of the experiment, immediately after the solute was injected in the apparatus, some solute remained in well W5, and was then introduced into the apparatus when glycerin was injected into the apparatus through well W5 during Flow Step 1. Thus, the peak mass in the apparatus occurs at the end of Flow Step 1. Flow Step 2 is an extraction step, during which some solute mass is extracted from well W5, reducing mass over the flow step. Most of the extracted mass remained in the well and was reinjected during Flow Step 3, leading to an increase in mass during Flow Step 3. Finally, solute mass was extracted at well W5 through the extraction during Flow Step 4.

In the present study, we focus on the radial movement of the solute. Radial solute distributions were obtained from the images in Fig. 3 using radialavg.m in Matlab (Fischer 2019), and are shown in Fig. 5. The radial plumes exhibit Gaussian-like behavior, with the plume moving outward during the injection flow steps (Flow Steps 1 and 3, which have injection at well W5) and inward during the extraction flow steps. The spreading is due to (1) nonuniform movement of the solute as it flows around beads, (2) velocity variations within a pore, and (3) differential velocities through pores of varying sizes as a result of slight variations in bead packing. When the solute concentration is averaged in the vertical direction (through the imaging method) and in the angular direction (using radialavg.m), this variability in flow paths manifests as apparent mechanical dispersion at the Darcy scale. As explained above, the molecular diffusion coefficient



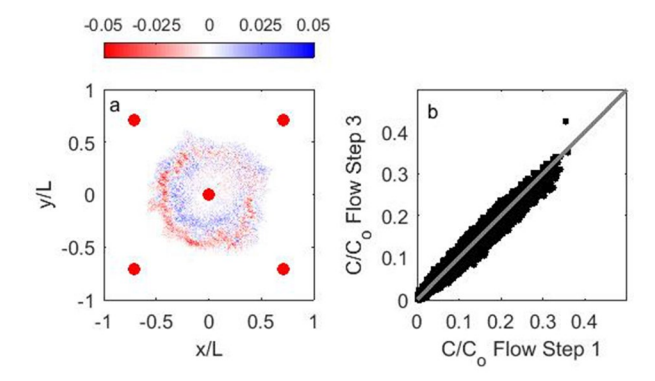
of Rhodamine 6G in glycerin is sufficiently low that molecular diffusion is negligible during the short duration of the experiment, so all spreading is due to mechanical dispersion.

Since the mass of solute in the test cylinder at the end of each flow step is approximately equal (i.e., only a small amount of the dye is removed from well W5 during the extraction steps), the areas under each curve in Fig. 5b are all approximately equal. Thus, the curve with the highest maximum concentration (red curve, for Flow Step 2) has the least amount of spreading, and the curves with the lowest maximum concentration (blue and yellow curves, for Flow Steps 1 and 3, respectively) have the most spreading. One notable observation from Fig. 5 is that the amount of spreading is dependent on the radial distance from well W5, rather than the travel time. In particular, the radial plumes at the end of Flow Steps 1 and 3 are located at the same distance from well W5, since Flow Step 3 injects fluid at the same rate that fluid was extracted during Flow step 2. The radial plumes at the end of Flow Steps 1 and 3 are nearly identical, even though the solute has been in the test cylinder three times longer at the end of Flow Step 3 than at the end of Flow Step 1. Figure 6 compares the two-dimensional dye plumes at the end of Flow Steps 1 and 3 (Fig. 3b,d). Figure 6a shows the difference in normalized concentration at each pixel. The differences are, in general, less than 10% of the actual values measured at each pixel (See Fig. 3b,d). The mean value of the difference in normalized concentration is  $2.1 \times 10^{-4}$  and the standard deviation of 0.0059. Figure 6b shows a scatterplot of normalized concentrations for each pixel at the of Flow Steps 1 and 3. All of the data fall close to the 1:1 line, with a correlation coefficient of 0.996. This quantitative analysis confirms that the dye distributions at the end of Flow Steps 1 and 3 are nearly identical. This behavior suggests that the flow paths at the pore scale are completely reversible, and consequently, the spreading at the Darcy scale is also completely reversible. In the next section, we use numerical simulations to investigate this behavior.

## 3 Numerical Investigation

In this section, we use numerical simulations to reproduce the radial plume movement that was observed in the experiment. The velocity variations within the pore space manifest as mechanical dispersion on the Darcy scale. We show that the Darcy scale spreading can be represented as a Fickian, reversible process.

Fig. 6 Comparison of normalized concentrations of dye plumes at the end of Flow Steps 1 and 3. a Difference between measured normalized concentration at the end of Flow Step 3 and at the end of Flow Step 1 for each pixel. b Normalized concentration at the end of Flow Step 3 vs. normalized concentration at the end of Flow Step 3 vs. normalized concentration at the end of Flow Step 1 for each pixel





## 3.1 Radial Flow and Transport Theory

Although flow in the experimental apparatus is not purely radial, the outer wells are sufficiently far from the solute plume such that flow is predominantly radial in the vicinity of the dye plume. Also, porosity varies in the radial direction (see Fig. 2c); however, it is essentially uniform for  $r > 2r_w$ . Assuming radial flow and uniform porosity, velocity, v(r, t), varies in the radial direction as

$$v(r,t) = \frac{dr}{dt} = \frac{Q(t)}{2\pi r h n} = \frac{Z(t)}{r}$$
(3)

where r is the radial distance from the center of the center well, t is time, Q(t) is the injection rate (Q < 0 represents extraction) into the test cylinder through well W5 at time t, b is the thickness of the apparatus, n is porosity, and  $Z(t) = Q(t)/(2\pi bn)$ . Storage is neglected, so changes in Q(t) lead to instantaneous changes in v(r, t).

Assuming dispersion is Fickian, the dispersive mass flux,  $J_d$ , is given by

$$J_{d} = -nD_{r}\frac{\partial C}{\partial r} = -n\alpha |v(r,t)|\frac{\partial C}{\partial r}$$

$$\tag{4}$$

where  $D_r = \alpha |v(r,t)|$  is the dispersion coefficient,  $\alpha$  is the dispersivity, and vertical bars denote magnitude. Using (3) and (4), solute transport can be represented with the radial advection-dispersion equation, given by

$$\frac{\partial C}{\partial t} + \frac{Z(t)}{r} \frac{\partial C}{\partial r} = \alpha \frac{|Z(t)|}{r} \frac{\partial^2 C}{\partial r^2}$$
 (5)

where C(r, t) is solute concentration as a function of radial position r and time t. We solve (5) using random walk particle tracking, in which the position of particle  $\ell$  at time step j+1,  $r_{\ell,j+1}$ , is obtained from

$$r_{\ell,j+1} = \sqrt{r_{\ell,j}^2 + \frac{Q^j \Delta t}{\pi b n}} + \sqrt{\frac{\alpha |Q^j| \Delta t}{\pi b n r_{\ell,j}}} \epsilon_{\ell,j}$$
 (6)

where  $r_{\ell j}$  is the position of particle  $\ell$  at time step j,  $Q^j$  is the injection rate into the test cylinder at time step j,  $\Delta t$  is the time step,  $\epsilon_{\ell j}$  is a random deviate drawn from a Gaussian distribution with zero mean and unit variance. The first term on the right-hand side of (6) represents the new position due to advection, which is found by integrating (3) for constant Q, while the second term represents the random dispersion step (Dentz et al 2015). The values of  $Q^j$  used in (6) are related to the injection and extraction rates through well W5 that are reported in Table 1, but they are not identical. Let  $N^*$  be the number of time steps in each flow step. Then  $Q^j$  is given by

$$Q^{j} = f_{b} f_{O} Q_{5,J} \text{ for } (J-1)N^{*} < j \le JN^{*}$$
(7)

where J is the flow step number,  $f_b = 13/16$  is a thickness correction factor that is the ratio between the imaged thickness (thickness over which C is measured, i.e., 13 bead layers) and the actual thickness (thickness over which fluid is injected or extracted, i.e., 16 bead layers), and  $f_Q$  is a flow correction factor that adjusts for other discrepancies, such as, for example, short circuiting of flow along the upper face of the apparatus.



To obtain concentration, the particles were binned by position into bins of size  $\Delta r$ . The concentration of each bin was obtained using

$$C_k = \frac{m_p N_k}{2\pi b n_k r_k \Delta r} \tag{8}$$

where  $C_k$ ,  $N_k$ ,  $n_k$  and  $r_k$  are the concentration, number of particles, porosity, and radial distance to the center of bin k, respectively. Here we use the spatially-varying porosity. Finally the resulting distribution was smoothed through convolution with a zero-mean Gaussian with a standard deviation of  $\Delta r$ .

The maximum mass of solute in the test cylinder was  $M_{\rm max}=0.1325$  mg, occurring at the end of Flow Step 1 (Fig. 4). The mass was uniformly distributed over  $N_p=200,000$  particles, giving each particle a mass of  $m_p=6.623\times 10^{-7}$  mg. At t=0, the test cylinder contained 0.1038 mg of solute (Fig. 4); thus, the initial solute distribution was represented by 156,745 particles that were randomly distributed to approximate the experimental radial dye distribution at t=0, shown in Fig. 7. The same initial particle distribution was used in all simulations. The remaining particles were introduced during simulation of Flow Step 1, with introduction times randomly chosen to match the red dashed line in Fig. 4, which approximates the measured distribution.

During all injection flow steps, any particles that were dispersed into well W5 were reflected back into the domain. During extraction flow steps, particles that entered well W5 were removed for the duration of the extraction flow step. Particles that were extracted in Flow Step 2 were reintroduced into the domain during the next injection step, Flow Step 3. Figure 4 shows that mass in the test cylinder increases approximately linearly during Flow Step 3, so these particles were reintroduced at random times drawn from a uniform distribution between the starting and ending times of Flow Step 3.

#### 3.2 Numerical Simulation Results

Equation (5) was solved using (6) to replicate the solute plume movement of the experiment, with  $Q^i$  defined in (7). All parameters are known except for the flow correction factor  $f_Q$  and the dispersivity  $\alpha$ , which were manually adjusted to match the peak concentration, location of the peak concentration, and width of the simulated and experimental solute

Fig. 7 Simulated and experimental solute concentrations at t=0. The vertical dashed line represents the outer edge of well W5

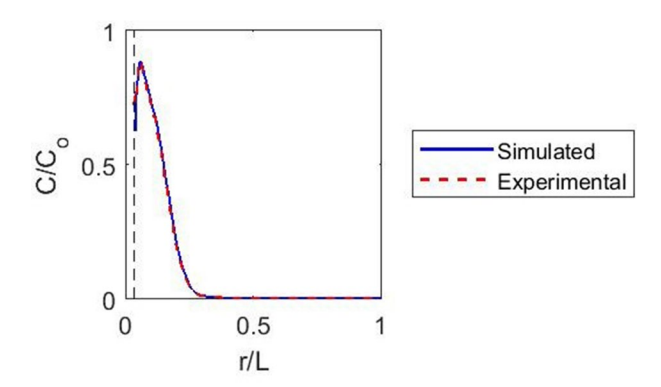




**Table 2** Parameter values used in the simulations

Parameter	Value	
Duration of each flow step	30 min	
Simulation time step, $\Delta t$	0.02 min	
Number of time steps in one flow step, $N^*$	1500	
Injection rate in well W5, $Q_{5,J}$		
Flow Step 1 $(J = 1)$	3.0 ml/min	
Flow Step 2 $(J = 2)$	-1.0 ml/min	
Flow Step 3 $(J = 3)$	1.0 ml/min	
Flow Step 4 $(J = 4)$	-0.5 ml/min	
Radius of test cylinder, L	11.6 cm	
Imaged thickness, b	3.58 cm	
Average porosity, n	0.311	
Number of particles, $N_p$	200,000	
Mass per particle, $m_p$	$6.623 \times 10^{-7} \mathrm{mg}$	
Spatial discretization, $\Delta r$	0.048 cm	
Thickness correction factor, $f_b$	0.8125	
Flow correction factor, $f_O$	0.9	
Dispersivity, $\alpha$	0.33 cm	

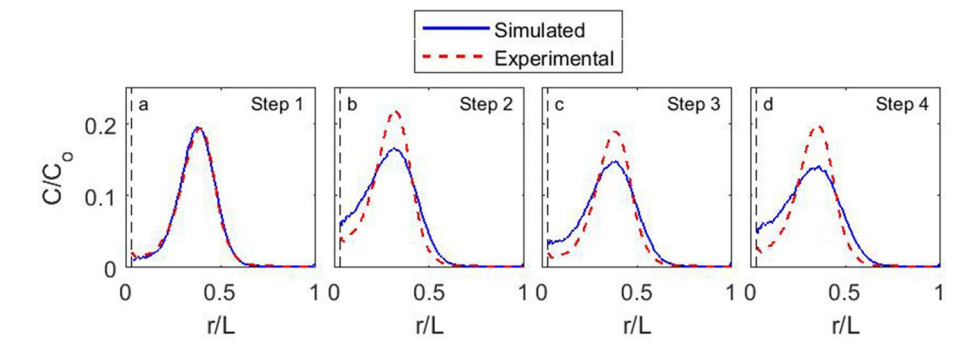


Fig. 8 Simulated and experimental solute concentrations at the end of Flow Steps 1–4 using normal Fickian dispersion. The vertical dashed line represents the outer edge of well W5

plumes at the end of Flow Step 1. The best-fit values of  $f_Q$  and  $\alpha$ , and known values of all other parameters, are presented in Table 2.

Figure 8 shows the simulated radial distributions of solute at the end of each flow step using these parameters. For comparison, the experimental results are also shown. At the end of Flow Step 1, the simulated plume is nearly identical to the experimental plume, supporting the Fickian dispersion model. At all later times, however, the simulated plume is much more disperse than the experimental results, suggesting that Darcy-scale dispersion does not follow a Fickian model.

To simulate the reduced spreading in the experiment, we tested two different models of modified Darcy-scale dispersion. In the first model, we eliminated dispersion in the extraction flow steps by setting  $\alpha=0$  in Flow Steps 2 and 4, thus simulating only advective movement during extraction flow steps. Both advection and dispersion were simulated in



Flow Steps 1 and 3 (injection flow steps). The results, shown in Fig. 9, show that the simulated plumes are still more disperse than the experimental results.

In the second model of modified Darcy-scale dispersion, the spreading that occurs during the injection Flow Steps (Flow Steps 1 and 3) is reversed in the extraction Flow Steps (Flow Steps 2 and 4). Spreading at the Darcy scale results from multiple flow paths taken by the solute as it moves around solid grains while it is advected outward during diverging, radial flow. When the flow direction is reversed, the solute retraces its path during inward, converging, radial flow. At the Darcy scale, this behavior manifests as reversible dispersion, i.e., the spreading during outward flow is undone during inward flow.

Implementing this reversible dispersion with particle tracking is carried out by storing the random deviates used in the injection Flow Steps, and reusing them in reverse order in the subsequent extraction Flow Steps and changing the sign. For example,  $\epsilon_{\ell,N^*+1} = -\epsilon_{\ell,N^*}$ . However, because the flow rates during extraction flow steps are lower than in the preceding injection flow steps (i.e.,  $|Q_{5,2}| < |Q_{5,1}|$  and  $|Q_{5,4}| < |Q_{5,3}|$ ), each random dispersion excursion would cover a larger distance during injection than during extraction. Thus, the same random deviate is used for multiple extraction time steps, with the number proportional to the ratio of the flow rates. For example,  $\epsilon_{\ell,N^*+1:N^*+3} = \epsilon_{\ell,N^*}$ ,  $\epsilon_{\ell,N^*+4:N^*+6} = \epsilon_{\ell,N^*-1}$ , etc., because the extraction rate in flow step 2 (which begins with  $j = N^* + 1$ ) is one third of the injection rate in flow step 1 (which ends with  $j = N^*$ ). Mathematically, this can be expressed by modifying (6) as

$$r_{\ell,j+1} = \begin{cases} \sqrt{r_{\ell,j}^2 + \frac{Q^j \Delta t}{\pi b n}} + \sqrt{\frac{\alpha |Q^j| \Delta t}{\pi b n r_{\ell,j}}} \epsilon_{\ell,j} & \text{for } 0 < j \le N^* \\ 2N^* + 1 < j \le 3N^* \\ \sqrt{r_{\ell,j}^2 + \frac{Q^j \Delta t}{\pi b n}} + \sqrt{\frac{\alpha |Q^j| \Delta t}{\pi b n r_{\ell,j}}} (-\epsilon_{\ell,j^*}) & \text{for } N^* + 1 < j \le 2N^* \\ \sqrt{r_{\ell,j}^2 + \frac{Q^j \Delta t}{\pi b n}} + \sqrt{\frac{\alpha |Q^j| \Delta t}{\pi b n r_{\ell,j}}} (-\epsilon_{\ell,j^{**}}) & \text{for } 3N^* + 1 < j \le 4N^* \end{cases}$$

$$(9)$$

where 
$$j^* = N^* + 1 - \lceil |Q_{5,2}|(j-N^*)/|Q_{5,1}| \rceil$$
 and  $j^{**} = 3N^* + 1 - \lceil |Q_{5,4}|(j-3N^*)/|Q_{5,3}| \rceil$ .

The results of the simulation with reversible dispersion, shown in Fig. 10, show that the simulated plumes match well with the experimental results. These results demonstrate

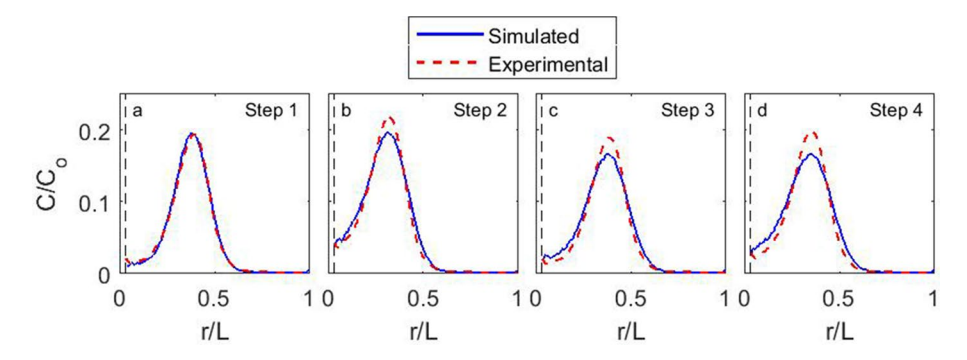


Fig. 9 Simulated and experimental solute concentrations at the end of Flow Steps 1–4 using  $\alpha = 0$  in extractions flow steps (Flow Steps 2 and 4). The vertical dashed line represents the outer edge of well W5



that the mechanical dispersion at the Darcy scale is reversed when the flow direction is reversed.

#### 4 Discussion

Experimental observations by de Anna et al (2014) and Gramling et al (2002) both demonstrated that upscaling concentrations of a single solute over multiple pores may lead to Fickian dispersion in the direction of flow. In the experiment by de Anna et al (2014), observed sub-pore concentrations were integrated over the direction transverse to flow in a two-dimensional Hele-Shaw cell; while in the experiment by Gramling et al (2002), upscaled concentrations were measured by integrating over the cross-sectional area perpendicular to flow in the three-dimensional rectangular column. In both cases, mean velocity was uniform, unidirectional, and steady. The results of the present experiment demonstrate that the behavior observed in these earlier studies also extends to steady, radial flow. Specifically, integrating concentration over the cross-sectional area perpendicular to flow (concentric cylinders) during Flow Step 1 (steady, radial outward flow) produced a one-dimensional upscaled concentration distribution in the flow (radial) direction that matches a Fickian model.

In this experiment, the imaging process measured the depth-averaged concentration; thus, we cannot resolve the pore-scale behavior. However, we can identify the patterns in the two-dimensional plumes that lead to apparent Fickian dispersion in the radial direction. Figures 11 and 12 show enlarged views of the porosity distribution (from Fig. 2b) and the two dimensional distribution of dye at the start of the experiment and at the end of Flow step 1, respectively, (from Fig. 3a,b, respectively), along with approximate travel paths (red dashed lines) from well W5 to 10 points labeled A–J. Along pathways that pass through predominantly high porosity regions (blue shading in Figs. 11a and 12a), the plume travels farther (Locations A, B, E, F, G, H), while along pathways that pass through low porosity regions (yellow shading), the plume does not travel as far (Locations D and I). Finally, we compare the width of the plume fringe (yellow shading in Figs. 11b and 12b). Near points C and J, the fringe is wide; whereas near A and F, the fringe is relatively narrow. Note that points C and J are in higher porosity regions than points A and F, and therefore have larger pores. The distribution of velocities is larger

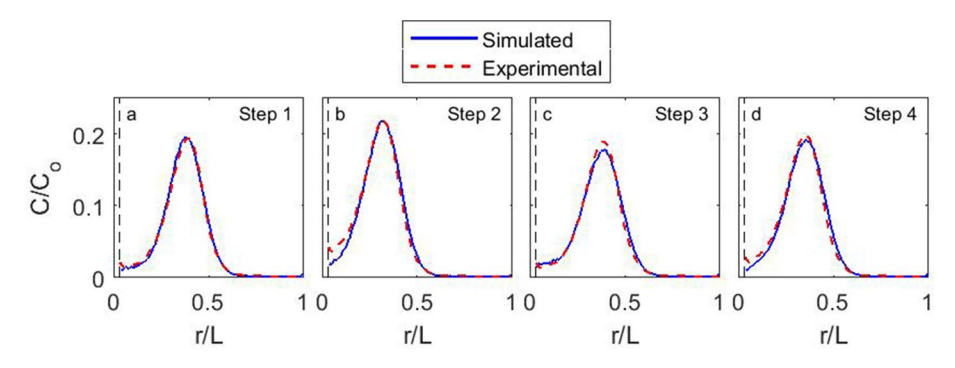
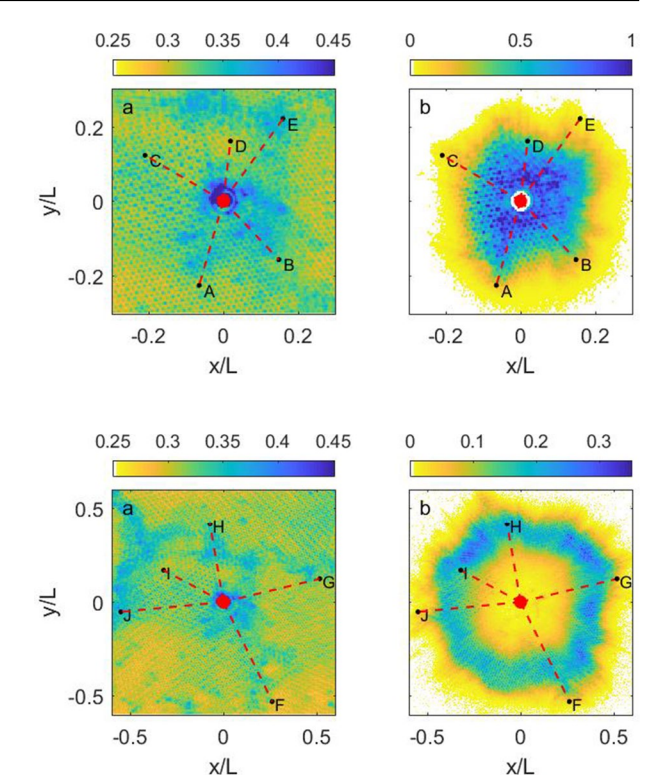


Fig. 10 Simulated and experimental solute concentrations at the end of Steps 1–4 using reversible dispersion. The vertical dashed line represents the outer edge of well W5

Fig. 11 a Porosity distribution and b normalized dye concentrations at the start of the experiment. Red dashed lines represent approximate travel paths from well W5 to the black circles labeled A–E which identify key features discussed in the text. The red circle represents well W5. Note that the spatial scale and the concentration color scale are different between this figure and Fig. 12



and **b** normalized dye concentrations at the end of Flow Step 1. Red dashed lines represent approximate travel paths from well W5 to the black circles labeled F–J which identify key features discussed in the text. The red circle represents well W5. Note that the spatial scale and the concentration color scale are different between this figure and Fig. 11

Fig. 12 a Porosity distribution

within a large pore then within a smaller pore; thus, the fringe is wider near C and J because of the larger distribution of solute travel distances as a result of the larger distribution of velocities within a pore. This behavior illustrates the differential velocities across pores of different sizes. Where porosity is high, and pores are relatively large, fluid velocities are higher and the plume travels farther. When these concentrations are averaged in the angular direction, the velocity variations manifest as spreading that can be represented by a Fickian model.

In this experiment, which has spherical and monodisperse granular media, porosity determines permeability through the Kozeny-Carman equation (Carman 1937). The nonuniform porosity indicates that the test cylinder is heterogeneous, and this heterogeneity leads to nonuniform propagation of dye in the radial direction. Similar nonuniform propagation has been observed in laboratory experiments with unidirectional flow in heterogeneous porous media (Zinn et al 2004; Oates and Harvey 2006; Yoon et al 2008). Since the heterogeneity in the push-pull experiment is generated through nonuniform distribution of pore sizes, the nonuniform propagation of the dye plume is dominated by pore-scale velocity variations. Although the pore-scale behavior cannot be resolved in this experiment, the pore-scale velocity variations will lead to fingering, which is equivalent to the formation of lamellae in a narrow band of dye in unidirectional flow (Le Borgne et al 2013, 2014). In unidirectional flow, the lamellae elongate as streamlines diverge around grains and eventually coalesce in a new pore (Le Borgne et al 2013). In outward radial flow, in which the bulk flow is diverging, fingers elongate as fluid flow around grains, but coalescence of the fingers is less prevalent. For example,



the outer boundary of the plume at the end of Flow Step 1 (Fig. 12b) is more erratic than the outer boundary of the plume at the start of the experiment (Fig. 11).

In steady flow, the lamellae growth leads to dispersion length scales of the upscaled concentrations that increase with time (Le Borgne et al 2013; Perez et al 2020). The results of the push-pull experiment show that dispersion length scales can decrease when flow reverses. The velocity field in this experiment is completely reversible. As fluid and solute are pushed outward during an injection step, the fluid velocity is high in the high porosity pathways and near the centers of the pores, and low in low porosity pathways and near the solid grain surfaces, leading to the uneven radial pattern of solute concentration shown in Fig. 3b. When solute concentrations are averaged vertically over the imaging thickness and in the angular direction to produce a radial distribution (blue line in Fig. 5), the resulting solute distribution is characterized by spreading in the radial direction, which can be represented as Fickian dispersion. As fluid and solute are pulled back to well W5 during an extraction step, the fluid velocity follows the same pattern of higher velocities through high-porosity pathways and low velocity through low-porosity pathways, reversing the solute spreading that occurred in the injection step. The resulting radial distribution of upscaled concentrations (averaged over the imaging thickness and angular direction) demonstrates apparent reversal of dispersion (red line in Fig. 5), a manifestation of nearly perfect reversal of flow.

Molecular diffusion of Rhodamine 6G in glycerin is slow relative to the duration of the experiment. Let us define the diffusion length scale as  $\ell = \sqrt{4Dt}$ , where t is the duration of the experiment. Using the molecular diffusion of Rhodamine 6G in glycerin of  $1.9 \times 10^{-9}$  cm<sup>2</sup>/s (Roth et al 2020), the diffusion lengths scale of Rhodamine 6G over the 120-minute experiment is  $\ell \approx 0.074$  mm, which is almost two orders of magnitude smaller than a bead diameter. Thus, over the duration of the experiment, the length scale of molecular diffusion is small compared to the pore size, and a negligible amount of solute diffuses off of its original streamline. Hence, as the flow field is reversed, nearly all of the solute follows its original travel path exactly, but in reverse. This result is analogous to the classic experimental demonstration of dye being mixed radially into glycerin, then un-mixed during reversed flow (Taylor 1967), and is an example of negligible mixing in the pore space. This negligible mixing is an extreme case of incomplete mixing, in which some, but not all, solute is exchanged across streamlines in the pores; thus, the spreading would be partially reversible upon flow reversal. Experimental evidence of incomplete mixing has been demonstrated previously (Raje and Kapoor, 2000; Gramling et al, 2002; de Anna et al, 2014), but to our knowledge, the present study is the first experimental study of incomplete mixing in radial flow, and the first to include flow reversal. Using the reversal of flow allowed for the identification of negligible mixing, based on the nearly identical plumes at the end of Flow Steps 1 and 3. Between the times represented by the end of Flow Step 1 and the end of Flow Step 3, fluid is first extracted and then reinjected for equal durations and at equal rates. If mixing were not negligible, additional apparent dispersion of the radial concentration would have been observed.

Kang et al (2015) presented a field push-pull test in a fractured material that demonstrated reversible dispersion. They separated transport processes into advective processes (e.g., advection, including separation of flow into multiple channels or fractures) and diffusive processes (e.g., matrix diffusion, hydrodynamic dispersion, adsorption). Advection processes can be partially reversible when the flow field is reversed (Kang et al 2015). In the present study, although transport appears to follow a Fickian dispersion model at the Darcy scale, the transport is based entirely on advective processes, which were fully reversible in this experiment, since molecular diffusion was negligible.



The diffusion length scale in a field remediation system would be longer than the diffusion length scale in this experiment, due to longer time scales and higher diffusion coefficients in water. For example, the diffusion coefficient for Rhodamine 6G in water is  $4 \times 10^{-6}$  cm<sup>2</sup>/s (Gendron et al 2008), which is about three orders of magnitude higher than for Rhodamine 6G in glycerin, as was used in the experiment. Using this diffusion coefficient, the diffusion length scale,  $\ell = \sqrt{4Dt}$ , over a 30-day remediation period would be about 60 mm, which is much larger than the typical pore size. Thus, a much higher degree of mixing would be observed in the field, and a reversal of flow would not produce the reversal of dispersion as was observed in the experiment. However, in fractured media, a reversal of flow can lead to partial reversal of dispersion even at the field scale (Kang et al 2015).

### 5 Conclusions

Rhodamine 6G dye concentrations were measured during a push-pull experiment in a  $50 \text{ cm} \times 50 \text{ cm} \times 4.4 \text{ cm}$  apparatus filled with monodisperse glass beads and glycerin. Because of the low molecular diffusion coefficient of Rhodamine 6G in glycerin, molecular diffusion was negligible during the 120-minute experiment; thus, the pore-scale transport was dominated by advection. The imaging method observed the depth-averaged concentrations (averaged over several pores in the vertical dimension), and post-processing of the depth-averaged concentrations led to upscaling of the concentrations over the angular dimension. The resulting radial distribution of dye concentration was replicated with particle tracking in a one-dimensional radial direction, which simulated advection and dispersion. The apparent dispersion of the upscaled model was a manifestation of variable velocities within a single pore and across pores. The results show that the upscaled concentrations in the radial direction follow a Fickian dispersion model during steady, outward radial flow, consistent with other studies in steady, unidirectional flow.

Because molecular diffusion was negligible, advection of dye was completely reversible during the push-pull experiment, with dye moving radially outward during the push phase, and following the same path in reverse during the pull phase. This reversal led to apparent reversible dispersion of the upscaled concentrations. We developed a new particle tracking approach to simulate the reversible dispersion. The reversible dispersion is an indication of incomplete mixing in the pores, for the specific situation here of negligible molecular dispersion, which produces negligible mixing in the pore space.

**Supplementary Information** The online version contains supplementary material available at https://doi.org/10.1007/s11242-021-01682-3.

**Author Contributions** All authors contributed to the study conception and design. Material preparation and collection of experimental data were performed by Eric J. Roth, under the supervision of John P. Crimaldi. Analysis of experimental data was performed by Eric J. Roth and Roseanna M. Neupauer. Numerical simulations were performed by Roseanna M. Neupauer. The manuscript was written by Roseanna M. Neupauer, and all authors commented on previous versions of the manuscript. All authors read and approved the final manuscript.

Funding This research was funded by the National Science Foundation under Grants EAR-1417005 and EAR-1417017.

Data Availability The datasets used in the current study are available from the corresponding author on request.



**Code Availability** No specialized code was used in this study.

#### **Declarations**

**Conflict of interest** The authors have no conflicts of interest to report.

#### References

- Carman, P.C.: Fluid flow through granular beds. Trans. Inst. Chem. Eng. 15, 150–166 (1937)
- de Anna, P., Dentz, M., Tartakovsky, A., Le Borgne, T.: The filamentary structure of mixing fronts and its control on reaction kinetics in porous media flows. Geophys. Res. Lett. **41**(13), 4586–4593 (2014). https://doi.org/10.1002/2014GL060068
- Dentz, M., Kang, P., Le Borgne, T.: Continuous time random walks for non-local radial solute transport. Adv. Water Resour. 82, 16–26 (2015). https://doi.org/10.1016/j.advwatres.2015.04.005
- Fischer, D.: radialavg.zip. https://www.mathworks.com/matlabcentral/ fileexchange/46468-radia lavg-zip(2019)
- Gendron, P.O., Avaltroni, F., Wilkinson, K.J.: Diffusion coefficients of several rhodamine derivatives as determined by pulsed field gradient-nuclear magnetic resonance and fluorescence correlation spectroscopy. J. Fluoresc. 18(6), 1093–1101 (2008). https://doi.org/10.1007/s10895-008-0357-7
- Gramling, C.M., Harvey, C.F., Meigs, L.C.: Reactive transport in porous media: A comparison of model prediction with laboratory visualization. Environ. Sci. Technol. 36(11), 2508–2514 (2002). https://doi. org/10.1021/es0157144
- Kang, P.K., LeBourne, T., Dentz, M., Bour, O., Juanes, R.: Impact of velocity correlation and distribution on transport in fractured media: Field evidence and theoretical model. Water Resour. Res. 51, 940–959 (2015). https://doi.org/10.1002/2014WR015799
- Le Borgne, T., Dentz, M., Villermaux, E.: Stretching, coalescence, and mixing in porous media. Physical Review Letters 110(20):https://doi.org/10.1103/PhysRevLett.110.204,501(2013)
- Le Borgne, T., Ginn, T.R., Dentz, M.: Impact of fluid deformation on mixing-induced chemical reactions in heterogeneous flows. Geophys. Res. Lett. 41(22), 7898–7906 (2014). https://doi.org/10.1002/2014G L062038
- Oates, P.M., Harvey, C.F.: A colorimetric reaction to quantify fluid mixing. Experiments in Fluids 41:673–683. https://doi.org/10.1007/2Fs00348-006-0184-z(2006)
- Perez, L.J., Hidalgo, J.J., Puyguiraud, A., Jiménez-Martínez, J., Dentz, M.: Assessment and prediction of pore-scale reactive mixing from experimental conservative transport data. Water Resources Research 56:e2019WR026,452, https://doi.org/10.1029/2019WR026452(2020)
- Raje, D.S., Kapoor, V.: Experimental study of bimolecular reaction kinetics in porous media. Environ. Sci. Technol. 34, 1234–1239 (2000). https://doi.org/10.1021/es9908669
- Roth, E.J., Neupauer, R.M., Mays, D.C., Sather, L.J., Crimaldi, J.P.: Wall effect mitigation techniques for experiments with planar walls. Transp. Porous Media 132, 423–441 (2020). https://doi.org/10.1007/ s11242-020-01399-9
- Roth, E.J., Mays, D.C., Neupauer, R.M., Sather, L.J., Crimaldi, J.P.: Methods for laser-induced fluorescence imaging of solute plumes at the Darcy scale in quasi-two-dimensional refractive index-matched porous media. Transp. Porous Media 136, 879–898 (2021). https://doi.org/10.1007/s11242-021-01545-x
- Taylor, G.: Film notes for low-Reynolds-number flows, p. 21617. National Committee for Fluid Mechanics Films, Education Development Center, Inc No (1967)
- Yoon, H., Zhang, C., Werth, C.J., Valocchi, A.J., Webb, A.G.: Numerical simulation of water flow in three dimensional heterogeneous porous media observed in a magnetic resonance imaging experiment. Water Resources Research 44,(2008). https://doi.org/10.1029/22007WR006213
- Zinn, B., Meigs, L.C., Harvey, C.F., Haggerty, R., Peplinski, W.J., von Schwerin, C.F.: Experimental visualization of solute transport and mass transfer processes in two-dimensional conductivity fields with connected regions of high conductivity. Environ. Sci. Technol. 38(14), 3916–3926 (2004). https://doi.org/10.1021/es034958g

**Publisher's Note** Springer Nature remains neutral with regard to jurisdictional claims in published maps and institutional affiliations.

